Supporting Information for

Titanium nitride as a promising sodium-ion battery anode: Interface-confined preparation and electrochemical investigation

Ming Liu[a], Zilu Zhang[b], Yunyun Xie[b], Zhiwei Guo[a], Hua Feng[a], Wenyou Liu[a], Hai Wang[a,b,c]

Corresponding author. E-mail: hbwanghai@gmail.com (H. Wang)

[a] College of Physics and Technology, Guangxi Normal University, Guilin 541004, China

[b] College of Materials Science and Engineering, Guilin University of Technology, Guilin 541004, China

[c] State Key Laboratory of Optoelectronic Materials and Technologies, Sun Yat-sen University, Guangzhou, 510275, China

Table of Contents

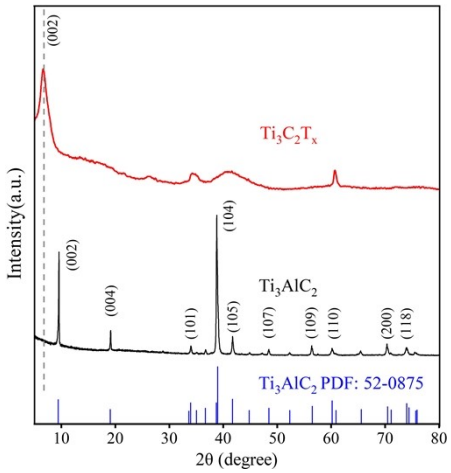

Figure S1. XRD patterns of Ti_3AlC_2 and $Ti_3C_2T_x$.

MXene nanosheets were obtained by optionally etching the metal Al layer in Ti_3AlC_2 (Figure S1). For the Ti_3AlC_2 powder, the main diffraction peaks situated at 9.5° and 38.8° was fitted well with those of Ti_3AlC_2 (JCPDS 52-0875), corresponding to its (002) and (104) planes,[1] respectively, which. After etching Ti_3AlC_2 by HCl/LiF, there was a significant decrease in the crystallinity of $Ti_3C_2T_x$. The disappearance of the peak located at 2θ=38.8° indicates successful etching of the Al layer,[2] and the peak at 2θ = 9.5° migrated to 6.61°, indicating that the layer spacing expands from 9.86 Å to 13.36 Å.[3]

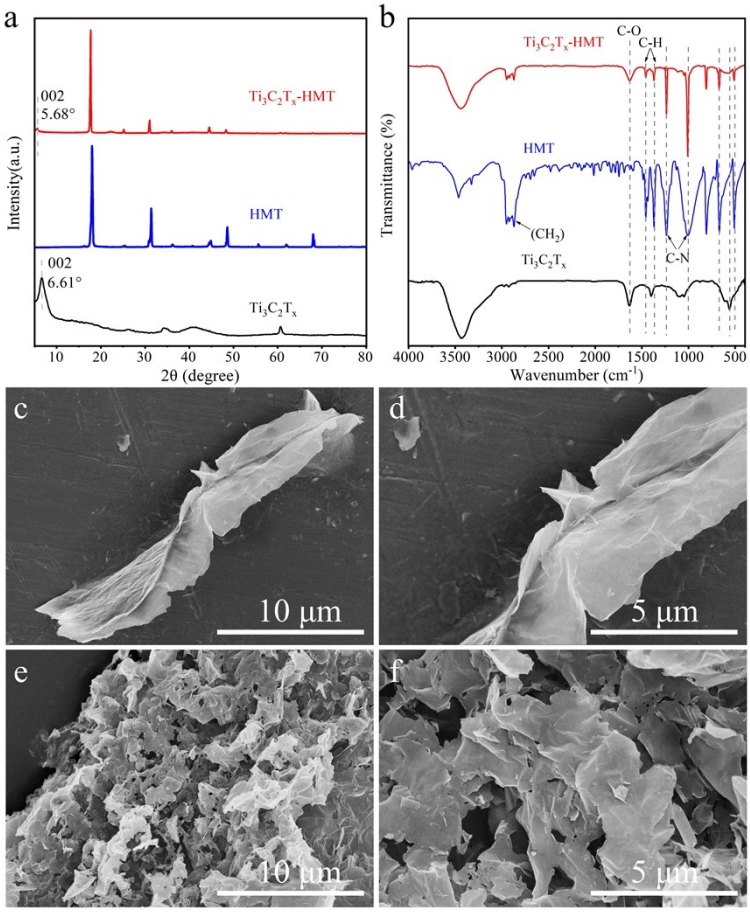

Figure S2. (a) XRD patterns of $Ti_3C_2T_x$, HMT and $Ti_3C_2T_x$-HMT; (b) FTIR spectra of $Ti_3C_2T_x$, HMT and $Ti_3C_2T_x$-HMT, and their FESEM images of $Ti_3C_2T_x$ (c, d); $Ti_3C_2T_x$-HMT (e, f).

Figure S2a shows the successful insertion of amines into $Ti_3C_2T_x$ substrates via the HMT treatments. The characteristic peak at 2θ=6.61° shifting to 5.68° corresponded to the interplanar spacing of 15.54 Å. It is thus reasonable to explain that due to electrostatic interactions, The HMT molecules occupying the interlayer space orient themselves with the protonated NH^{4+} end pointing toward the $Ti_3C_2T_x$ layers, which were consistent with previous report.[4] The results show that HMT ligands successfully ligated with $Ti_3C_2T_x$ species. In FTIR spectrum (Figure S2b), the two strong absorption bands of $Ti_3C_2T_x$-HMT at 1000 cm^{-1} and 1225 cm^{-1} can be assigned to the fundamental

plane of the C-N stretching vibration.[5] In addition, the FTIR spectra diffraction pattern of $Ti_3C_2T_x$-HMT nanosheets was significantly different from that of $Ti_3C_2T_x$, further confirming the successful preparation of $Ti_3C_2T_x$-HMT.

To understand the morphological of $Ti_3C_2T_x$ and $Ti_3C_2T_x$-HMT, we made further FESEM analysis (Figure S2c-f). Obviously, there is no residual bulk MAX in the few-layer MXene (Figure S2c and d) and the exfoliated MXene nanosheets displayed flat and smooth. Figure S2e and f shows a typical FESEM images of the obtained 2D MXene-HMT composite nanosheets. The morphologies of MXene changed significantly before and after the combination with HMT. After adding HMT, MXene changed from a continuous nanosheet to a fragment, but still maintained the raw 2D morphologies, and here MXene played the role of a symbiotic template.

Note1. XRD analysis of TiN formation.

As shown in Figure 2b, the XRD comparative patterns of the $Ti_3C_2T_x$/C-300, $Ti_3C_2T_x$/C-500, and TiN/C show the temperature dependence of the crystal structure change from MXene/C to TiN/C. The result shows that $Ti_3C_2T_x$-HMT can successfully transform to TiN (PDF: 87-0633) via a simple heating process at 800 ℃. Notably, the XRD diffractogram of the TiN/C composite exhibited a weak peak at ca 22.4°, which was associated with the (002) plane of carbon with low graphitization.[6] Further, it is found that the crystallinity of MXene/C-500 sample is significantly better than that of MXene/C-300. The results show that with the increase of temperature, the structural reorganization occurs between MXene and C layer, which may be related to the atomic diffusion at the interface between MXene and carbon layer. When the temperature

raised to 800 °C, we can infer fast diffusion of the N atoms on the Ti surface of MXene led to the formation of TiN that remained covalently bonded to carbon matrix via Ti-C bonding.

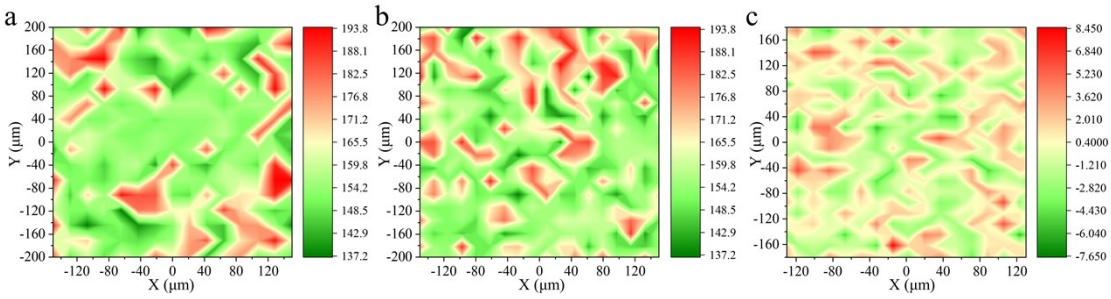

Figure S3. Raman mapping of (a) $Ti_3C_2T_x$/C-300, (b) $Ti_3C_2T_x$ /C-500 and (c) TiN/C for a 300 × 400 μm^2 areas.

Raman spectral imaging was a powerful tool that was based on a detailed chemical image generated from the Raman spectrum of a sample. From Raman imaging we can obtain the distribution of sample components, particle size; changes in crystallinity in the sample, phase changes; contaminant particle size and shape; interactions and mixing of boundary components of different phases; stress distribution in the sample.[7] Raman spectra of $Ti_3C_2T_x$ and carbon show clear features that do not overlap, which provided important information on the distribution of the two components, this contributes to the understanding of $Ti_3C_2T_x$/C composites.[8] The Raman data have been reorganized into intensity mapping, and Figure S3a, S3b and S3c show the Raman mapping images of the $Ti_3C_2T_x$/C-300, $Ti_3C_2T_x$/C-500 and TiN/C. Taking Figure S3c as an example, high intensity "green" areas indicate the presence of carbon layers, while "red" areas are associated with the presence of Ti. The color distribution in the Figure S3a-c and is relatively uniform, which confirms the distributed carbon layer is uniform.

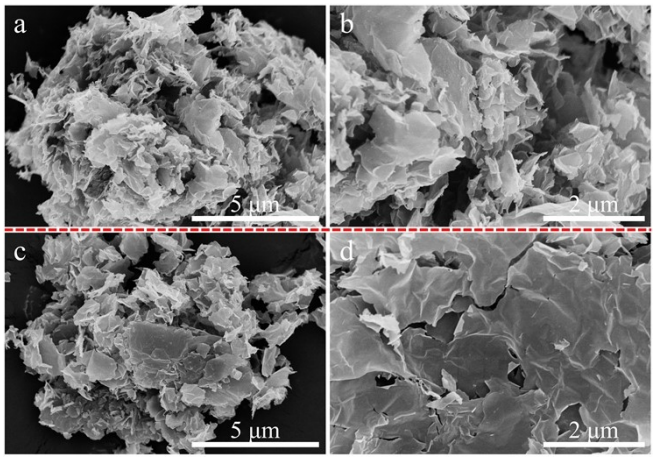

Figure S4. (a, b) SEM images of $Ti_3C_2T_x$/C-300; (c, d) SEM images of $Ti_3C_2T_x$/C-500.

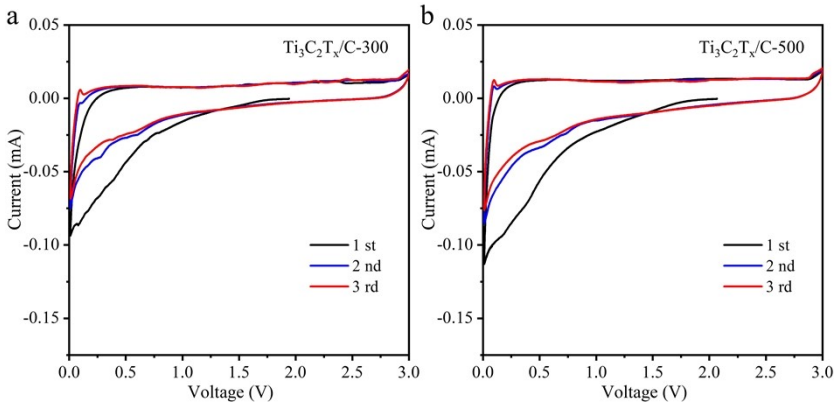

Figure S5. Cyclic voltammogram of the electrodes during the first three cycles at 0.1 mV s^{-1}. (a) $Ti_3C_2T_x$/C-300 and (b) Ti_3C_2Tx/C-500.

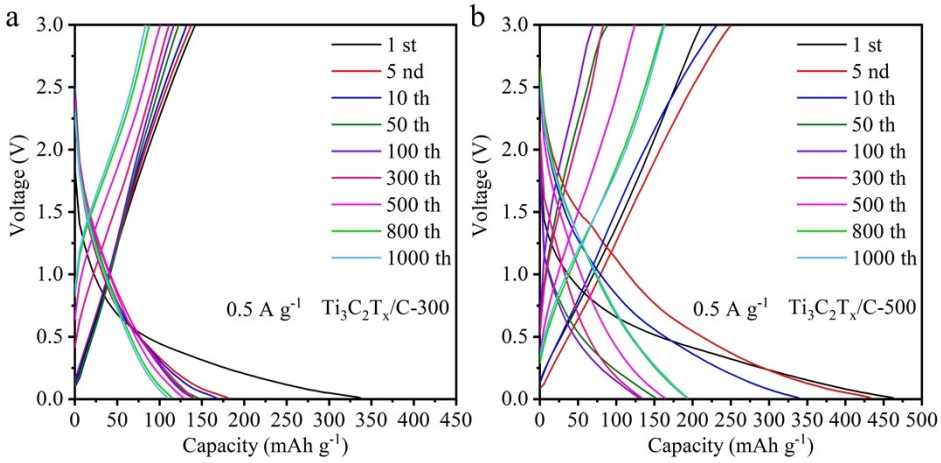

Figure S6. The voltage profile of $Ti_3C_2T_x$/C-300 and $Ti_3C_2T_x$/C-500 electrodes at different cycles. (a) $Ti_3C_2T_x$/C-300 and (b) $Ti_3C_2T_x$/C-500 at 0.5 A g^{-1}.

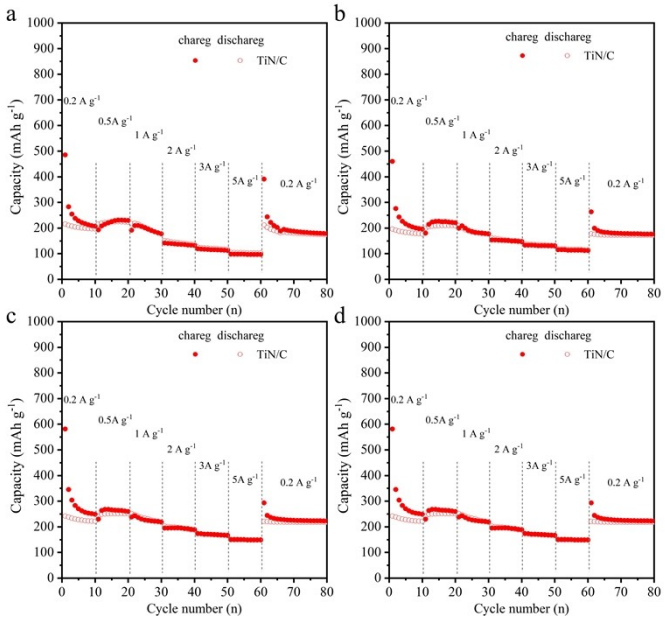

Figure S7. Rate performance of TiN/C electrodes at different current densities.

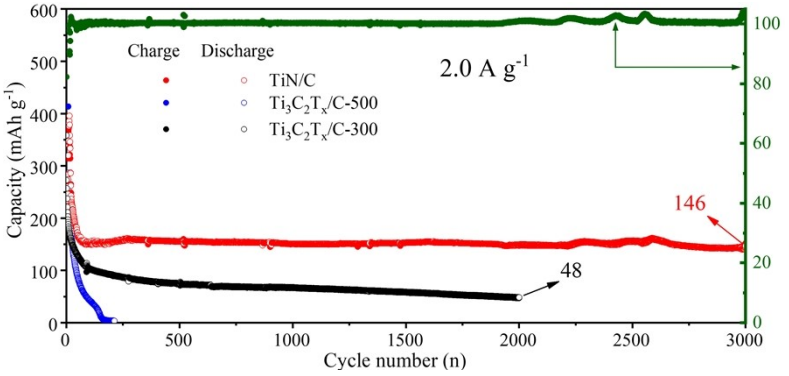

Figure S8. The long cycling performance of $Ti_3C_2T_x$/C-300, $Ti_3C_2T_x$/C-500 and TiN/C anodes at 2 A g^{-1} after 5000 cycles.

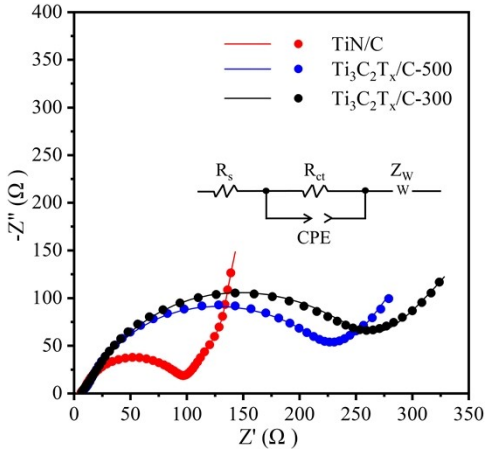

Figure S9. EIS of $Ti_3C_2T_x$/C-300, $Ti_3C_2T_x$/C-500 and TiN/C anodes and equivalent circuit (inset).

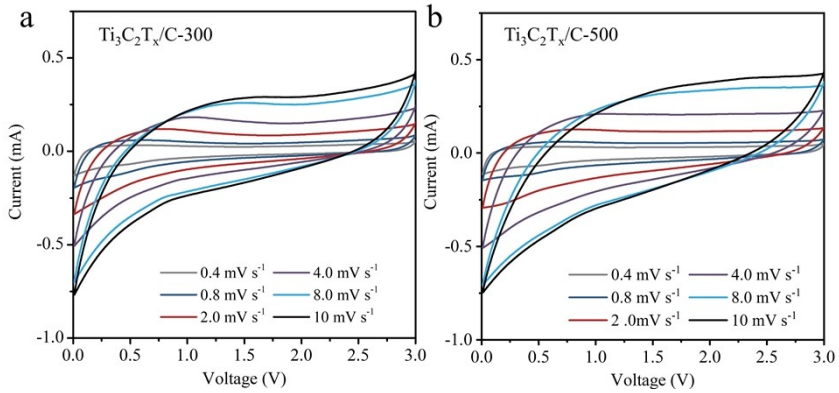

Figure S10. The CV curves at different scan rates CV curves (a) $Ti_3C_2T_x$/C-300, (b) $Ti_3C_2T_x$ /C-500 anode.

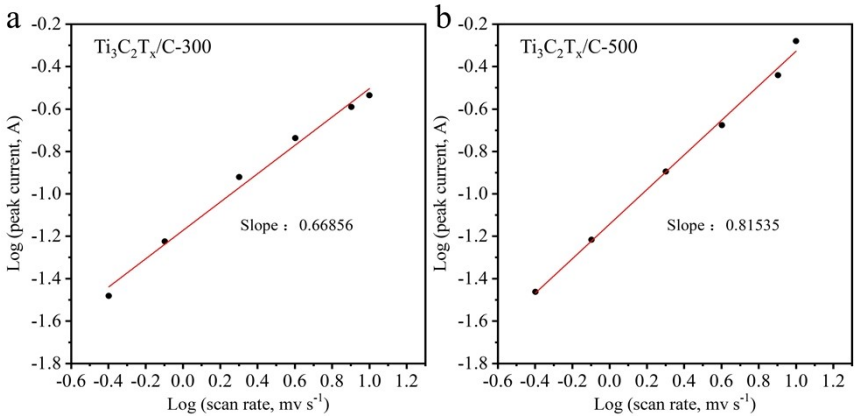

Figure S11. Logarithmic peak current vs. logarithmic scan rate (a) $Ti_3C_2T_x$/C-300, (b) $Ti_3C_2T_x$ /C-500 anode.

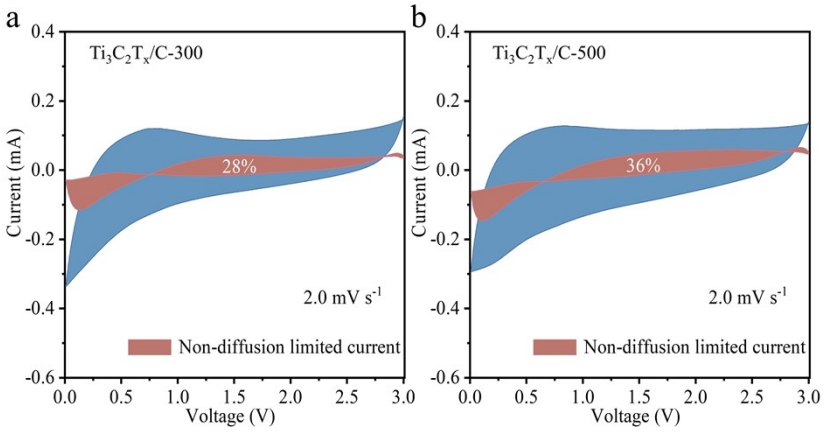

Figure S12. (a) the contribution of pseudocapacitance to the total $Ti_3C_2T_x$/C-300 current at a scanning rate of 2.0 mV s^{-1} (red and pink areas), (b) the contribution of pseudocapacitance capacitance to the total $Ti_3C_2T_x$/C-500 current at a scanning rate of

2.0 mV s^{-1} (red and pink areas).

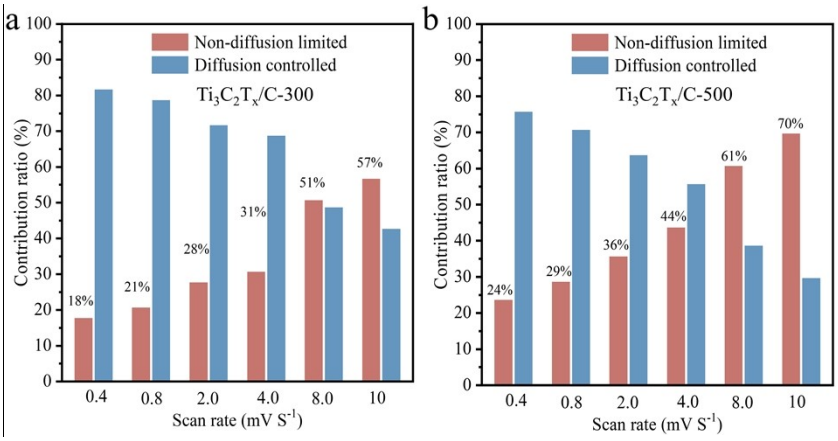

Figure S13. Percentage capacitive contributions at different scanning rates of $Ti_3C_2T_x$/C-300 (a) and $Ti_3C_2T_x$/C-500 (b) at a scan rate of 0.4, 0.8, 2.0, 4.0, 8.0 and 10 mV s^{-1}.

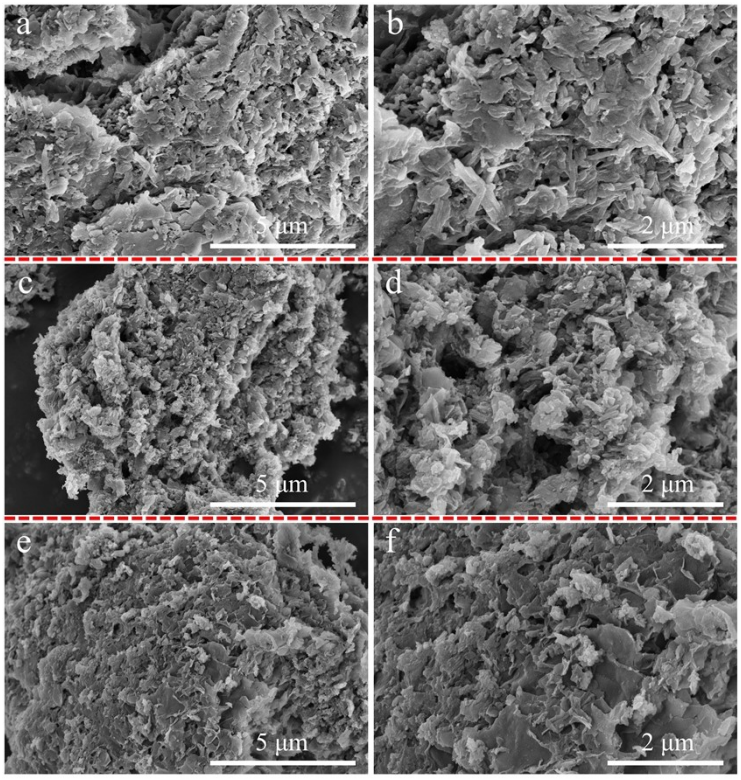

Figure S14. SEM images of $Ti_3C_2T_x$/C-300 (a-b), $Ti_3C_2T_x$/C-500 (c-d) and TiN/C (e-f) after 50 cycles at 0.5 A g^{-1}.

Table S1. Specific surface area (SBET), total pore volume and mean pore size of

$Ti_3C_2T_x$/C-300, $Ti_3C_2T_x$/C-500 and TiN/C.

Samples	Specific surface area (m^2 g^{-1})	Adsorption pore volume (cm^3 g^{-1})	Desorption pore volume (cm^3 g^{-1})	Adsorption pore size (nm)	Desorption pore size (nm)
$Ti_3C_2T_x$/C-300	41.67	0.048	0.066	4.65	6.23
$Ti_3C_2T_x$/C-500	70.66	0.079	0.072	4.12	4.72
TiN/C	99.33	0.12	0.14	4.84	5.46

The surface area and porosity of the three samples were studied from the adsorption isotherm of N_2 (77 K).The Brunauer-Emmett-Teller (BET) specific surface areas of $Ti_3C_2T_x$/C-300, $Ti_3C_2T_x$/C-500 and TiN/C were 41.67, 70.66 and 99.33 m^2 g^{-1}, respectively (Table S1). The BET SSA of TiN/C is remarkably high compared with the values $Ti_3C_3T_x$ and porous carbon composites. This high SSA, together with the TEM, XRD and Raman results, can be attributed to the formation of unaggregated quantum-sized TiN and porous carbon.

Mesoporous properties were also confirmed by N_2 gas adsorption, which show type IV adsorption with H1 lag loops according to IUPAC classification.[9] Moreover, the pore size distribution (PSD) shows that TiN/C indicated higher pore volume (0.12 cm^3 g^{-1}) than $Ti_3C_2T_x$/C-300 (0.048 cm^3 g^{-1}) and $Ti_3C_2T_x$/C-500 (0.079 cm^3 g^{-1}) (Table S1). The increased surface area of TiN/C contributed to improved electrolytic accessibility and thus overall electrochemical performance.[10]

Table S2. XPS peak fitting results of TiN and their binding energies, atomic concentrations and assignments.

region	atomic concentration (%)	BE (eV)	assigned to	fraction of individual components (%)
C 1s	54.16	284.80	C-C	0.344185
		282.05	C-Ti	0.173056
		285.79	C-N	0.375832
		288.74	C-O	0.106928
N 1s	14.10	397.11	N-Ti	0.332302
		400.95	Quaternary-N	0.193076
		398.57	C-N=C	0.316323
		396.19	N-Ti-O	0.158299
O 1s	11.98	529.88	Ti-O	0.257253
		530.26	C=O	0.389093
		531.81	C=O/C-O-C	0.353697
Ti 2p	16.83	455.18	Ti-C	0.33233
		461.23	Ti-N	0.171483
		457.83	Ti-O	0.193042
		463.75	Ti $2p_{1/2}$	0.09948
		456.70	Ti^{2+} $2p_{3/2}$	0.134403
		462.51	Ti-C/Ti-O	0.069262
F 1s	2.92			

Table S3. XPS peak fitting results of $Ti_3C_2T_x$/C-300 and their binding energies, atomic concentrations and assignments.

region	atomic concentration (%)	BE (eV)	assigned to	fraction of individual components (%)
C 1s	50.19	284.80	C-C	0.498829
		285.91	C-N	0.321379
		281.24	C-Ti	0.128636
		285.50	C=O	0.051156
N 1s	17.90	398.01	pyridine	0.606089
		399.76	C-N	0.393911
O 1s	10.79	532.00	C-O	0.200486
		528.65	Ti-O-Ti	0.49557
		529.89	Ti-O-Ti	0.303944
Ti 2p	10.04	453.89	Ti^{3+} $2p_{3/2}$	0.325854
		459.83	Ti^{4+} $2p_{1/2}$	0.167921
		458.06	Ti^{4+} $2p_{3/2}$	0.053844
		463.52	Ti^{3+} $2p_{1/2}$	0.027747
		455.32	Ti^{2+} $2p_{3/2}$	0.280226
		461.01	Ti^{2+} $2p_{1/2}$	0.144408
F 1s	11.07			

Table S4. XPS peak fitting results of $Ti_3C_2T_x$/C-500 and their binding energies, atomic concentrations and assignments.

region	atomic concentration (%)	BE (eV)	assigned to	fraction of individual components (%)
C 1s	54.44	284.80	C-C	0.416999
		285.94	C-N	0.35631
		281.68	C-Ti	0.137165
		288.61	C=O	0.089526
N 1s	15.12	400.70	C-N=C	0.446829
		398.54	pyridine	0.553171
O 1s	14.76	529.56	Ti-O-Ti	0.299449
		530.12	Ti-O	0.249873
		531.94	C=O	0.450678
Ti 2p	11.84	455.97	C-Ti	0.397061
		461.90	Ti^{3+} $2p_{1/2}$	0.204616
		457.74	Ti $2p_{3/2}$	0.141607
		463.75	Ti $2p_{1/2}$	0.072974
		454.94	Ti^{3+} $2p_{3/2}$	0.121772
		460.87	Ti^{3+} $2p_{1/2}$	0.06197
F 1s	3.83			

Table S5. Cell parameters of TiN and TiO.

Samples	Crystalline system	a (Å)	b (Å)	c (Å)
TiN	Orthorhombic PDF: 87-0633	4.238	4.238	4.238
TiO	Orthorhombic PDF: 86-2352	4.293	4.293	4.293

Table S6. Comparison of TiN/C with competitive MXene-driven anodes and TiO_2 anodes for Na-ion batteries.

Anodes	Cycle stability			Ref.
	Current density (mA g^{-1})	Cycles (n)	Charge capacity (mAh g^{-1})	
This work	500	5000	170	
	1000	5000	149	
	2000	3000	146	
T-MXene@C	1000	3000	139	11
S-doped $Ti_3C_2T_x$	100	100	183	12
$Ti_3C_2T_x$/CNT-SA	20	100	175	13
$Na_{0.23}TiO_2/Ti_3C_2T_x$	2000	4000	56	14
3D microporous film	500	1000	295	15
TiO_2/C nanofibers	200	1000	237	16
NC-TiO_2/MXene	2000	1900	157	17
carbon-coated anatase p-doping TiO_2	1000	2000	115	18
porous hierarchical TiO_2/MoS_2/RGO nanoflowers	100	100	610	19

Table S7. Electrochemical data derived from EIS spectra for $Ti_3C_2T_x$/C-300, $Ti_3C_2T_x$ /C-500 and TiN/C.

Samples	**R_s (Ω)**	**R_{ct} (Ω)**
$Ti_3C_2T_x$/C-300	5.94	213.2
$Ti_3C_2T_x$/C-500	5.97	179.5
TiN/C	5.39	76.16

References:

1 Y. Wang, Y. Li, Z. Qiu, X. Wu, P. Zhou, T. Zhou, J. Zhao, Z. Miao, J. Zhou and S. Zhuo, *J. Mater. Chem. A*, 2018, 6, 11189-11197.

2 M. Naguib, M. Kurtoglu, V. Presser, J. Lu, J. Niu, M. Heon, L. Hultman, Y. Gogotsi and M. W. Barsoum, *Adv. Mater.*, 2011, 23, 4248-4253.

3 M. Naguib, O. Mashtalir, J. Carle, V. Presser, J. Lu, L. Hultman, Y. Gogotsi and M. W. Barsoum, *ACS Nano*, 2012, 6, 1322-1331.

4 Mashtalir, M. R. Lukatskaya, M. Q. Zhao, M. W. Barsoum and Y. Gogotsi, *Adv. Mater.*, 2015, 27, 3501-3506.

5 S. Liu, J. Zhou and H. Song, *Adv. Energy Mater.*, 2018, 8, 1800569.

6 Y. Yuan, T. Wang, H. Chen, S. M. Mahurin, H. Luo, G. M. Veith, Z. Yang and S. Dai, *Angew. Chem. Int. Ed.*, 2020, 59, 21935-21939.

7 M. S. Dresselhaus, A. Jorio, M. Hofmann, G. Dresselhaus and R. Saito, *Nano Lett.*, 2010, 10, 751-758.

8 M. Couzi, J.-L. Bruneel, D. Talaga and L. Bokobza, *Carbon*, 2016, 107, 388-394.

9 Svidrytski, D. Hlushkou, M. Thommes, P. A. Monson and U. Tallarek, *J. Phys. Chem. C*, 2020, 124, 21646-21655.

10 R. Pérez, S. H. Yeon, J. Ségalini, V. Presser, P. L. Taberna, P. Simon and Y. Gogotsi, *Adv. Funct. Mater.*, 2013, 23, 1081-1089.

11 P. Zhang, R. A. Soomro, Z. Guan, N. Sun and B. Xu, *Energy Storage Mater*, 2020, 29, 163-171.

12 J. Li, D. Yan, S. Hou, Y. Li, T. Lu, Y. Yao and L. Pan, *J. Mater. Chem. A*, 2018, 6, 1234-1243.

13 X. Xie, M.-Q. Zhao, B. Anasori, K. Maleski, C. E. Ren, J. Li, B. W. Byles, E. Pomerantseva, G. Wang and Y. Gogotsi, *Nano Energy*, 2016, 26, 513-523.

14 J. Huang, R. Meng, L. Zu, Z. Wang, N. Feng, Z. Yang, Y. Yu and J. Yang, *Nano Energy*, 2018, 46, 20-28.

15 M. Q. Zhao, X. Xie, C. E. Ren, T. Makaryan, B. Anasori, G. Wang and Y. Gogotsi, *Adv. Mater.*, 2017, 29, 1702410.

16 Y. Xiong, J. Qian, Y. Cao, X. Ai and H. Yang, *ACS Appl. Mater. Interfaces.*, 2016, 8, 16684-16689.

17 F. Wang, X. Ma, P. Zou, G. Wang, Y. Xiong, Y. Liu, F. Ren and X. Xiong, *Surf. Coat. Technol.*, 2021, 422, 127568.

18 Z. Guan, K. Zou, X. Wang, Y. Deng and G. Chen, *Chin. Chem. Lett.*, 2021.

19 J. Ma, M. Xing, L. Yin, K. San Hui and K. N. Hui, *Appl. Surf. Sci.*, 2021, 536, 147735.